Electron and positron backscattering in the medium-energy range

G. R. Massoumi, W. N. Lennard, and Peter J. Schultz
The Positron Beam Laboratory,
Department of Physics, The University of Western Ontario, London, Ontario, Canada N6A 3K7

A. B. Walker
School of Physics, University of East Anglia, Norwich NR4 7TJ, United Kingdom

Kjeld O. Jensen
Department of Physics, University of Essex, Colchester CO4 3SQ, United Kingdom
(Received 24 November 1992)

Experimental data for positron and electron backscattering from thick solids are presented as a function of incident and outgoing angles and energies, and of target atomic number. A full description of the experimental features and limitations is presented. The data are compared with Monte Carlo calculated backscattering distributions, and in all cases the agreement is extremely good. Specularlike scattering for positrons incident at oblique angles is observed and explained in terms of the strength of the elastic-scattering interaction.

I. INTRODUCTION

Doubly differential studies of the angle and energy of backscattered electrons from solids have been of interest for many years, largely due to the use of energetic electron probes in analytical materials science applications such as Auger electron spectroscopy, or scanning and transmission electron microscopy. Of more fundamental scientific importance, the combined study of electron (e^-) *and* positron (e^+) backscattering provides a rare opportunity to establish detailed interaction cross sections, since it is the simplest matter-antimatter system which can be routinely obtained and controlled in a modest laboratory.

There is a reasonable amount of experimental data available for electron backscattering, representing a large range of incident projectile angles and energies, target species, and experimental geometries [see, for example, Neidrig's review and references therein].[1-7] There has, however, been very little experimental work concerned with positron backscattering at intermediate energies (10–100 keV), before the recent flurry of activity in this area.[8-12] Theoretical treatments[13-16] and analytical expressions[17] for the basic positron scattering interactions predate experiment by many years, although results are still far from consistent. More detailed and precise experimental information about macroscopic effects, in particular the energy and angular distribution of backscattered particles, is required to establish the validity of existing theories.

In this paper, we present a compendium of our recent experimental and theoretical investigations of electron and positron backscattering from different thick targets with atomic numbers in the range $4 \leq Z \leq 82$. Data measured for various experimental conditions are presented, including studies of total backscattering probabilities, dependence on material and incident-beam energy, and detailed differential studies for various angles of incidence over the range $0° \leq \alpha \leq 80°$. There is a dearth of prior measurements for comparison with our positron backscattering data, although data for electrons are compared where appropriate with other published results.[2-5] Monte Carlo computer simulations are compared with the experimental data, and the agreement is remarkably good. The simulations are also used to investigate the details of the backscattering process through an examination of particle histories. Some of the experimental and theoretical results presented in this paper have been published elsewhere in preliminary or abbreviated form.[8,9,18]

II. EXPERIMENT

A schematic of the apparatus used to measure electron and positron backscattering yields and energy spectra is shown in Fig. 1. The facility is described in more detail elsewhere.[18,19] Energetic positrons from an isotopic ^{58}Co or ^{22}Na source were moderated in solid Ar, from which they are emitted with $\sim 14.2 \pm 1.7$-eV energy.[20] The positron beam was formed in a modified Soa gun[21] and electrostatically guided through a Heddle five-element afocal lens,[22] a home-built electrostatic accelerator, and a final focusing Einzel lens—with the beam spot less than 3-mm in diameter. The electron beam was produced using a standard electron gun in place of the positron source and moderator. Beam intensities were kept to less than 10^4 Hz to facilitate single-event counting. It was found that under normal conditions a stability of better than 0.2% in projectile intensity could be achieved during each measurement.

Samples were mounted on a multitarget holder at the center of a small target chamber, which also housed a retractable channel-electron multiplier array (CEMA) used for beam alignment and diagnostics. A rotatable, energy-dispersive surface-barrier detector (SBD) was used

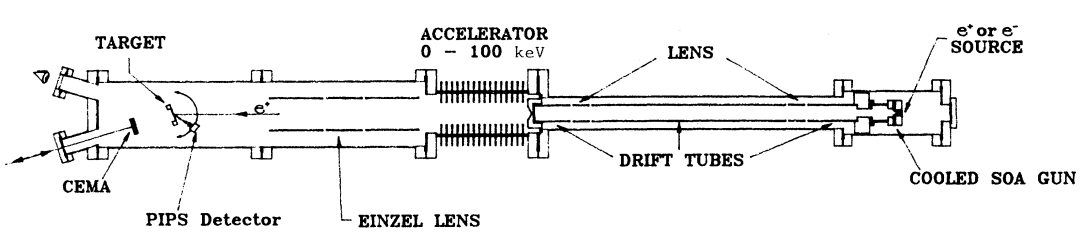

FIG. 1. Overview of the University of Western Ontario (UWO) electrostatically guided positron beam.

for most measurements of backscattered particles, although when necessary it was replaced by a second CEMA, used for low-energy positron or electron detection. Two different surface-barrier detectors were employed, which were 100 and 150 μm partially depleted PIPS (passivated implanted planar silicon) with active (circular) areas of 25 and 50 mm^2, respectively. The larger-area detector was used for most measurements. The positron beam apparatus and target chamber had a base pressure of about 5×10^{-8} Torr, which was found to be necessary for the routine growth of an efficient moderator.[19]

Figure 2 illustrates the experimental geometry. The target could be tilted by an angle α, defined as the angle of the surface normal ($\hat{n}$) relative to the incident-beam direction ($-\hat{k}$). The SBD was rotatable in the same plane (defined by $\hat{k}$ and $\hat{n}$), where γ is the angle of the SBD relative to $\hat{n}$, which therefore had values in the range $-90\leq\gamma\leq90°$ (irrespective of the sample tilt angle, α). Positive angles correspond to the clockwise direction when viewed from above (Fig. 2). Due to geometrical constraints introduced by the SBD mounting hardware, γ was restricted to regions exceeding $\pm30°$ relative to the incident beam, $\hat{k}$. For the sample-to-detector distance of 42 mm used, the solid angle subtended by the active area of the larger (50 mm^2) SBD was $\Omega_d=28$ msr, yielding a half angle of 5.4°. Periodically, the target was retracted and the detector moved to $\theta=0°$ (where θ is the scattering angle) to measure the incident intensity rate I_0.

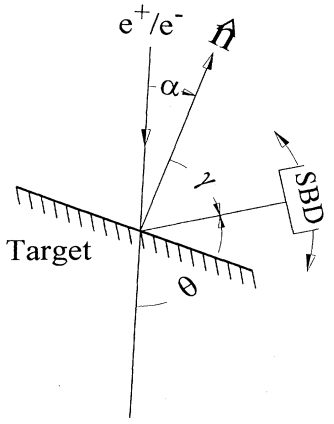

FIG. 2. Schematic of the experimental geometry.

The samples—all better than 99.5% and in most cases 99.99% purity—were cleaned in alcohol prior to mounting on the target holder, i.e., no *in situ* cleaning was attempted. At the energies of interest, the penetration depth of the average electron or positron which is eventually backscattered is much greater than the expected thickness of any native oxide layer. In addition, all samples used in the measurements can be regarded as "thick," since their thicknesses were much greater than the range of the incident projectiles. The physical dimensions of the samples were as large as (or exceeded) $\sim15\times15$ mm^2.

Doubly differential backscattering data $d^2\eta/d\Omega dE$ were measured for both positrons and electrons at normal *and* tilted angles of incidence. Total intensities for the differential backscattered yields (integrated over energy), $d\eta(\gamma)/d\Omega$, were determined by measuring the ratio $I(\gamma)/I_0\Omega_d$. Due to detector noise limitations, the energy distributions could not be measured directly below $E_{\min}\sim15$ keV, which was approximately twice the detector electronic noise level. In order to derive the energy-integrated yield at a given angle, we assumed the intensity varied linearly with energy from $E=0$ up to $E_{\min}$. This assumption is supported by the Monte Carlo (MC) simulations. We estimate that the total uncertainty for each datum is $\sim10\%$ for $Z>20$, arising mainly from the integration procedures over the angle and energy. For $Z<20$, the uncertainties are larger due to the small yields and also due to the fact that a larger fraction of the backscattered positrons with low energies fall in the electronic noise region. Figures 3(a) and 3(b) show typical energy spectra—on a logarithmic scale—observed at $\theta=0°$ for 35 keV e^+ and e^-, respectively. The noise level limitation is evident in both spectra near channel ~25, i.e., the noise leads to increasing counts for channels less than approximately channel No. 25.

It was necessary to correct the absolute positron backscattering yields for a small contribution resulting from fast positrons that escape directly from the source. This background, determined for zero acceleration voltage, was subtracted from the raw spectra prior to analysis. In Fig. 3(a), the background due to backscattered fast positrons can be seen above channel No. ~150.

A second correction can arise due to backscattering from the detector itself. This effect cancels since it occurs for both the incident and backscattered fluxes and, to a very good approximation, both electron and positron

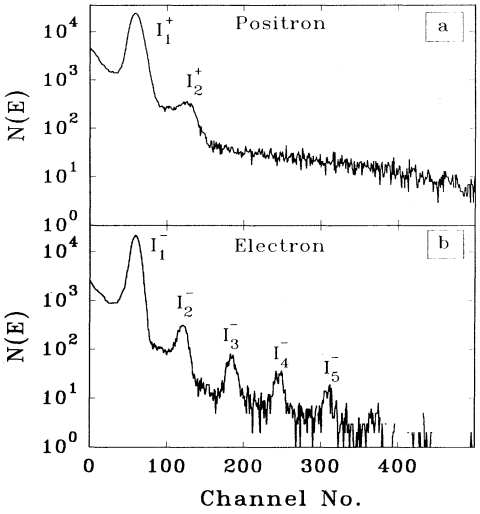

FIG. 3. (a) and (b): Logarithmic energy spectra for 35-keV positron and electron primary beams.

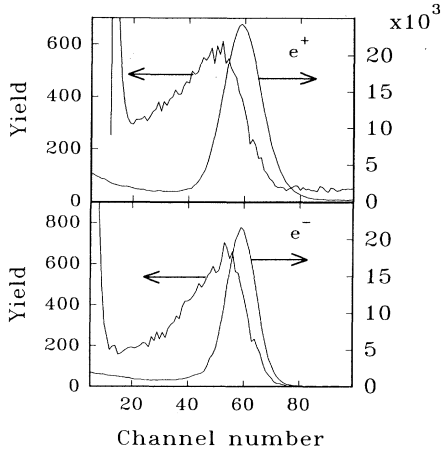

FIG. 4. (a) and (b): Energy spectra of backscattered positrons and electrons, compared with those for the primary beams.

backscattering coefficients are independent of energy over the 15–35 keV energy region that lies above the detector noise level.[13,14,18]

Finally, a correction due to pulse pileup in the detector must be considered in obtaining the energy-integrated yields. Pileup was only significant when measuring the incident flux, i.e., I_0, and not in the backscattered spectra because of the much lower count rates and low Ω. The correction procedure was more straightforward for positrons than for electrons. In Fig. 3(a), the peak labeled I_2^+ arises from pulse pileup, i.e., peaks appear at twice the incident energy due to two pulses arriving within the resolution time of the electronic system. Since its intensity relative to I_1^+ was small, $\sim 10^{-2}$, its integrated contribution was straightforward, and I_0^+ was then given by

$$I_0^+ = I_1^+ + 2I_2^+ \ . \tag{1}$$

Note that the fast e^+ background is subtracted first from the raw spectra *before* considering the pileup contribution.

For the electron case, there was an additional complication arising from the simultaneous acceleration of more than a single secondary electron. Thus, there appear in the 0° spectra peaks at multiples of the incident energy, see Fig. 3(b). These peaks represent events where, for example, two electrons arrive at the detector at *exactly* the same time. As well, there are pileup events contained in the peak appearing at twice the incident energy that originate for the same reason as in the positron case, i.e., two single secondary electrons arrive within the detection system resolving time. As far as the detector system is concerned, there is no difference in the resultant pulse-height distribution if two monoenergetic particles arrive at *exactly* the same time or at *nearly* the same time, where "nearly" implies within the system resolving time. The separate contributions to this peak at twice the incident energy can be evaluated from the positron data, since the total count rate was purposefully kept very nearly the same when recording data for both positrons and electrons. In the electron case I_0^- was given by

$$I_0^- = I_1^- + \sum_{k=2}^{N} kI_K^- \ , \tag{2}$$

where the pileup peaks are denoted by $k>1$. The backscattering coefficient η is then,

$$\eta^{+(-)} = \frac{I_r^{+(-)}}{\sum_{k=1}^{N} kI_k^{+(-)}} \ , \tag{3}$$

where $I_r^{+(-)}$ is the backscattered positron (electron) intensity. It should be noted that all of the terms discussed above result in a small ($<2\%$) correction, which appears somewhat exaggerated in the logarithmic plot shown in Fig. 3. The primary beams are shown again on a linear scale in Fig. 4, illustrating the $\sim$11-keV resolution of the surface-barrier detector. Also shown in Fig. 4 are typical distributions for backscattered positrons and electrons, in this case for Au with $\alpha=0°$ (normal incidence) and $\gamma=30°$.

III. MONTE CARLO CALCULATIONS

In the Monte Carlo (MC) simulations,[23] the trajectories of a large number of positrons (typically 10^5) were followed through the target material as they interact elastically and inelastically with the atoms and electrons. The inelastic scattering is described within the dielectric formalism, where the doubly differential inverse-mean-free path for a positron of momentum $\hbar k$ and mass m (equal to the free-electron mass), and hence energy $E=\hbar^2k^2/(2m)$, to undergo a scattering event with momentum transfer $\hbar q$ and energy loss $\hbar\omega$ is written as

$$\frac{d^2\tau(\omega,q,E)}{d\omega dq} = \frac{\hbar}{\pi E q a_0} \mathrm{Im}\left[\frac{-\epsilon_0}{\epsilon(q,\omega)}\right] \times \Theta(q-q_+)\Theta(q_+,q)\Theta(E-\hbar\omega) \ . \tag{4}$$

Here, τ is the inverse-mean-free path, $\epsilon(q,\omega)$ is the dielectric function for the medium, and $q_{\pm}=\sqrt{2m}\,(\sqrt{E}\pm\sqrt{E-\hbar\omega})/\hbar$ are the minimum and maximum momentum transfers allowed by energy and momentum conservation. Θ is the Heaviside step function, ϵ_0 the vacuum permittivity, and a_0 the Bohr radius. For $\mathrm{Im}(\epsilon_0/\epsilon)$, we have selected the model dielectric function proposed by Penn,[24] viz.,

$$\mathrm{Im}\left[\frac{\epsilon_0}{\epsilon(q,\omega)}\right]=\int_0^{\infty}d\omega' g(\omega')\mathrm{Im}\left[\frac{\epsilon_0}{\epsilon_L(q,\omega,\rho(\omega'))}\right]. \quad (5)$$

Here $\rho(\omega')=\epsilon_0 m(\omega'/e)^2$ is the electron-gas density corresponding to plasma frequency ω', ϵ_L is the Lindhard dielectric function for a free-electron gas of density ρ, and the weight function $g(\omega')$ is given by

$$g(\omega')=-\frac{2}{\pi\omega'}\mathrm{Im}\left[\frac{\epsilon_0}{\epsilon_{\mathrm{opt}}(\omega')}\right], \quad (6)$$

where $\epsilon_{\mathrm{opt}}(\omega)\equiv\epsilon(0,\omega)$ is the optical dielectric function. The full dependence of the scattering cross sections on E, ω, and q obtained from the Penn model are included in the simulations. The optical data $\epsilon_{\mathrm{opt}}(\omega)$ were taken from Ref. 25 and we include the full range of excitation energies from $\sim$0.1 eV to several keV; thus, the model accounts for both valence and core electron scattering including plasmon excitations. The elastic scattering was included using an expansion in partial waves, described in detail in Ref. 26. The atomic scattering potential was obtained from density functional calculations within the local spin-density approximation.

The simulations were performed for semi-infinite planar targets with atomic numbers in the range $13\le Z\le 79$ for normally incident particles and also for Al and Au targets for all angles of incidence. The positrons were followed until they either returned to the surface (backscattered positrons) or slowed down to an energy below 50 eV (implanted positrons). The exact choice of the termination energy did not affect the result since the backscattered intensity with energies below 100 eV is very low when the incident energy is $E_0=35$ keV.

IV. ELECTRON AND POSITRON BACKSCATTERING

A. Normal Incidence

Figure 5 shows the measured differential backscattering distributions $d\eta^{\pm}/d\Omega$ as a function of emission angle γ for 35-keV positrons and electrons at normal incidence on Al and Au targets. The upper curve shows positron data only (●) compared with MC simulations. The nearly linear dependence of $d\eta^{+}/d\Omega$ on $\cos\gamma$ is evident from the figure. In order to derive a total backscattering coefficient, we fitted the experimental data with a sum of Legendre polynomials and then integrated over the backward hemisphere (2π sr). The lower portion of Fig. 5 shows the positron (●) and electron (○) data together with the Legendre polynomial fits, shown as smooth solid curves.

Total backscattering coefficients for 35-keV positrons and electrons at normal incidence are shown in Fig. 6 as functions of target atomic number Z. We estimate that the total uncertainty for each datum is $\sim$10% for $Z>20$, arising mainly from the integrations over angle and energy as discussed earlier. For $Z<20$, the uncertainties are larger due to (i) the smaller yields, and (ii) a larger frac-

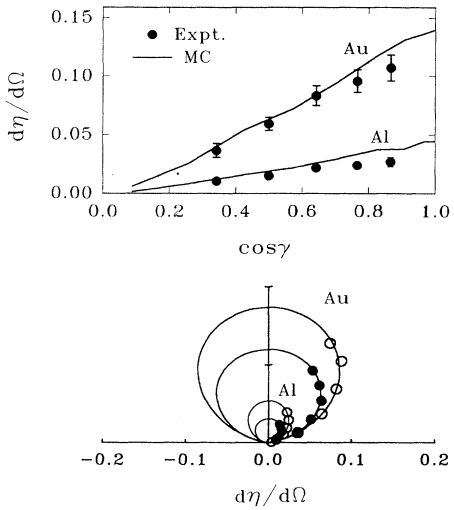

FIG. 5. Angular backscattering distributions, $d\eta^{\pm}/d\Omega$, for 35-keV positrons and electrons normally incident on Au and Al targets. The upper portion of the figure shows positron data (●) only compared with MC calculations (solid curve). The lower portion shows both positron (●) and electron (○) data together with the Legendre polynomial fit (smooth curve) used to calculate total backscattering coefficients from the data.

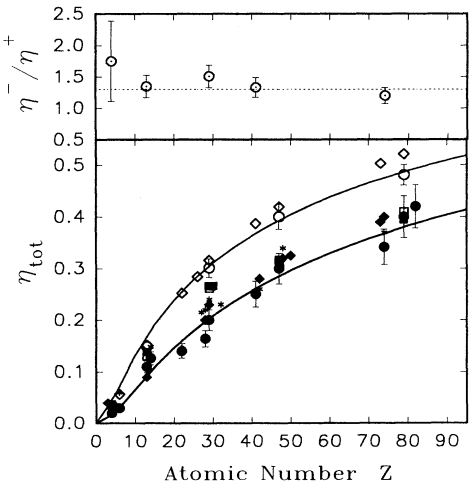

FIG. 6. Total backscattering coefficients $\eta_{\mathrm{tot}}^{\pm}$ as a function of target atomic number Z for positrons and electrons at normal incidence. ○ present electron data; ◇, electron data from Ref. 28; ●, present 35-keV positron data; ◆, positron data from Ref. 29; ■, positron data from Ref. 11; ★, positron data from Ref. 12; □, present MC positron results (35 keV). The upper portion shows the experimentally determined ratio η^{-}/η^{+} as a function of Z.

tion of the e^+ or e^- yield falling in the low-energy noise region of the SBD, as discussed in Sec. II. The smooth curves are fits to our data using the function $\eta(Z)=\exp(-AZ^{-1/2})$, where $A=8.59$ for positrons and $A=6.40$ for electrons. Arnal, Verdier, and Vincensini[27] derived the equation $\eta^-=1/(1+\cos\alpha)^p$ for the electron backscattering coefficient from bulk specimens from an empirical equation for the transmission coefficient of electrons, where $p=C/Z^{1/2}$ for normal incidence ($\alpha=0$). Using $C=9.4$, or $\eta^-=2^{-9.4/\sqrt{Z}}$ they obtained a good fit to electron experimental data in the energy region from 10 to 50 keV for a large range of target atomic numbers.[1] The two models are consistent with each other. Applying the model of Arnal and co-workers we obtain a visibly identical fit with $C\approx 9.2$ for electrons, and $C=12.4$ for positrons. Mäkinen *et al.* fit their 30-keV positron data with $C=11.5$.[12]

In addition to our own experimental results, all other related data from the literature are shown in Fig. 6. The criterion for comparison is that the experiment employed a beam of e^+ or e^- at normal incidence, as opposed to a "diffuse" or undefined geometry.[9] Our electron data points (○) are compared with the mean of data for 20-, 40-, and 60-keV electrons (◇), taken from Neubert and Rogaschewski.[28] Our positron data (●) are compared with data taken from Arifov, Grupper, and Alimkulov[29] (200-keV positrons; ◆), Coleman *et al.*[11] (35-keV positrons; ■), and Mäkinen *et al.*[12] (30-keV positrons; ★). The results of our MC calculations for 35-keV positrons are also shown (□). Our electron and positron measured values for total backscattering are given in Table I of Ref. 9.

Most of the data shown in Fig. 6 agree within the experimental uncertainties, both when comparing different sets of experimental data and between MC and experiment. The most significant discrepancy remaining in the positron data is near $Z=30$, which is not understood. Slight deviations from the monotonic increase with Z around $Z=30$ have been reported by Heinrich[30] and Mäkinen *et al.*[12] Our description of η vs Z is based on a simple structureless analytical expression, as has been done by other experiments.[31–33,12,1] While the quality of the experimental data does not justify a more detailed description at this time, there is in principle no *a priori* reason to expect a featureless dependence of η on Z, and the apparent experimental discrepancy near $Z=30$ may well be an indication of interesting new phenomena that have yet to be explored. Structure in this region has been predicted before, using a simple theoretical model.[34]

In the upper portion of Fig. 6, we show the experimentally determined ratio η^-/η^+ as a function of Z. It has long been thought that this ratio has a value ~ 1.3 over the entire periodic table, initially suggested by experiment,[31,32] as indicated by the horizontal dashed line. Although there may be some deviation from this simple ratio, our experimental data as well as others reported[11,12] still lack the precision to make any definitive statement to the contrary.

Experimental data for the total electron backscattering coefficient η^- at normal incidence for different materials and for incident energies in the range $5\le E_0\le 35$ keV are shown in Fig. 7.[18] Our data are compared with the data taken from Drescher, Reimer, and Seidel[6] (◇) and Neubert and Rogaschewski (▽).[28] Our measurements were performed using the CEMA, since it is more sensitive at low energies. The scattering angle for the detector was fixed at $\theta=150°$ (i.e., $\gamma=30°$). In the data analysis, it was assumed that the yield measured at this fixed angle was proportional to the total backscattered yield, and that the angular dependence was independent of the target Z. All values for these relative backscattering yields were made absolute by normalizing to data for 35-keV electrons incident on Au which were measured later using a SBD. The good agreement between our data and those of Refs. 6 and 28 confirms that indeed there is no significant Z dependence in the angular distribution within the energy range investigated, i.e., $\eta=K\,d\eta(150°)/d\Omega$, where K is a constant independent of Z. Here, the total backscattering coefficient is given by

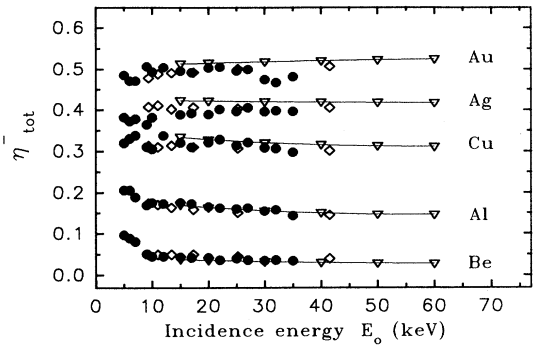

FIG. 7. Experimental data for the electron backscattering coefficient η^- vs incident energy E_0, for several different materials. ●, present electron data; ◇, electron data from Ref. 6; ▽, electron data from Ref. 28.

$$\eta^-=\int_{2\pi}(d\eta^-/d\Omega)d\Omega\ , \tag{7}$$

where the integration extends over the entire backscattering hemisphere.

B. Oblique incidence angles

Figures 8 and 9 show experimental results for angular backscattering distributions $d\eta/d\Omega$ for both 35-keV positrons and electrons and for different angles of incidence ($10°\le\alpha\le 60°$). The solid curves are the MC calculations for 35-keV positrons. The agreement between computational results and experiment is excellent, which is particularly encouraging in view of the fact that there are no adjustable parameters. It is noticeable that at lower incident angles, the distribution has the characteristic (approximate) cosine distribution that is observed for normal incidence.[1,2,5] As α increases, specular reflection becomes more evident for e^+ than for e^- for both Al and Au. Generally, at oblique incident angles, the backscattered intensity peaks near the reflection angle ($\alpha\approx\gamma$). In the case of Al (low Z), e^+ and e^- behave qualitatively the same. For Au, at $\alpha\ge 40°$ the electron and positron

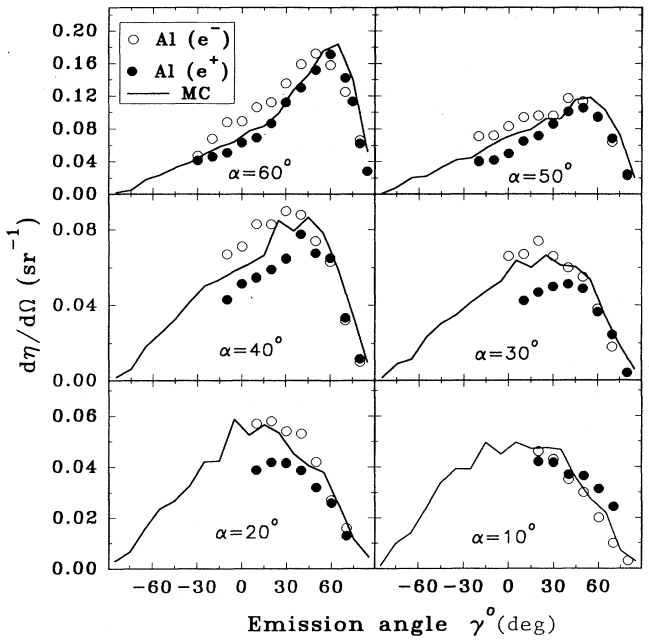

FIG. 8. Angular backscattering distributions $d\eta/d\Omega$ as a function of emission angle γ for the $\phi=0°$ plane for 35-keV positrons and electrons incident at different angles, $10° \leq \alpha \leq 60°$ on Al. The solid line shows the MC calculation for 35-keV positrons.

angular backscattering distributions behave neither qualitatively nor quantitatively the same.

The angular distribution of backscattered electrons is nearly symmetric about the surface normal, as illustrated clearly in Figs. 10 and 11 for our data (●). Also shown

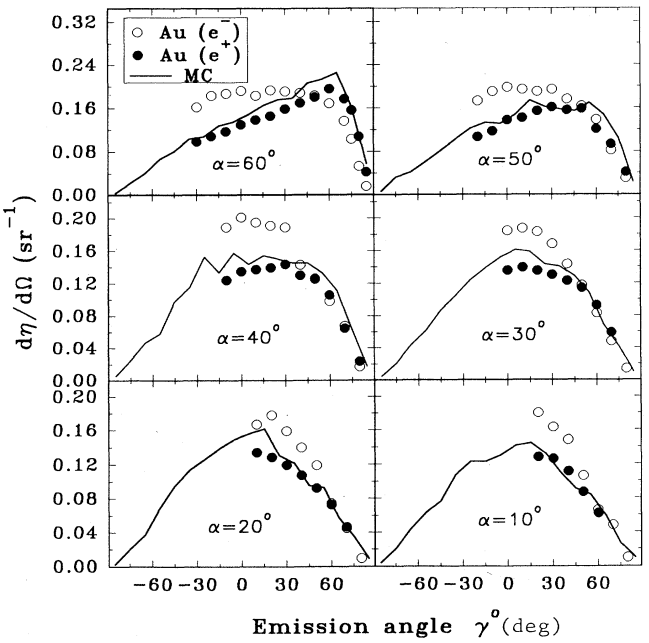

FIG. 9. Same as Fig. 8 for Au.

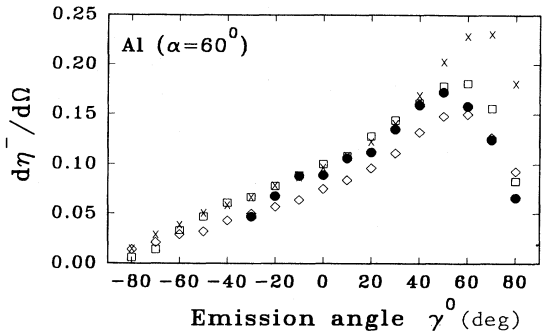

FIG. 10. Comparison of angular backscattering probabilities $d\eta^-/d\Omega$ from thick Al as a function of emission angle γ for electrons at a 60° angle of incidence. ●, present experimental electron data points, □, electron data from Ref. 4 (9.3 keV), ×, electron data from Ref. 5 (30 keV), ◇, electron data from Ref. 2 ($\alpha=55°$ and 50 keV).

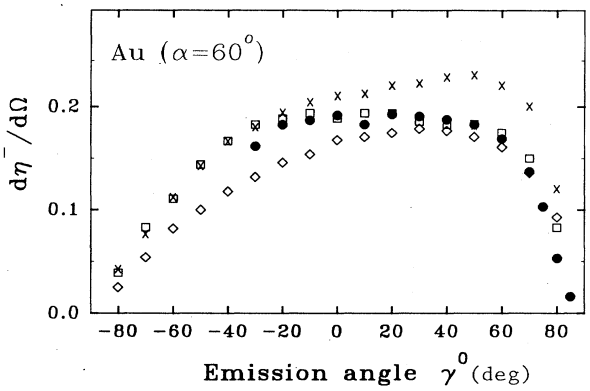

FIG. 11. Same as Fig. 10 for Au.

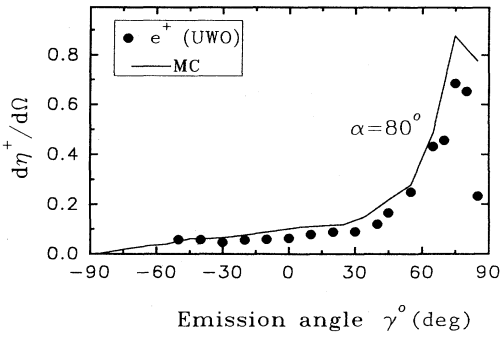

FIG. 12. Angular backscattering distributions for 35-keV positrons incident on Au at a glancing angle, $\alpha=80°$. Experimental and MC results are in good agreement.

are the data of Reimer, Pöpper, and Bröcker (□),[4] Darlinski (×),[5] and Kanter (◇).[2] The previously published data were digitized from the polar plots in the literature. The specular distribution evident in Figs. 8 and 9 for positrons at oblique angles of incidence is in sharp contrast with these electron data. This is even more pronounced for the positron data for a thick Au target at the extreme glancing incident angle, $\alpha = 80°$, as shown in Fig. 12. Although maximum effort was made to ensure that all positrons strike the sample, this is difficult at glancing angles due to the beam (~3-mm) diameter. However, the agreement between the experimental data and MC calculation is very good, providing support for the accuracy of the experimental data.

V. ENERGY DISTRIBUTIONS

Figure 13 shows the mean energy vs emission angle γ for backscattered positrons incident at 35 keV and $\alpha = 60°$ on Au and Al targets. The experimental data (●) are systematically lower than the MC results (□), but they follow the same trends for both Au and Al. There are small uncertainties associated with the experimental mean energy reflected by the error bars in Fig. 13. One source is the fact that the resolution function for the detector is not symmetric, but includes both pileup and incomplete charge collection events. The result is, on average, that any "true" event has a mean energy that is slightly reduced. Another potential source of error is the linear approximation described previously for the data which fall within the noise region of the detector (< 15 keV). Even with these errors considered, the experimental evidence suggests that there is slightly more energy lost during the backscattering process than predicted theoretically. This is consistent with the general trend for MC calculations to predict slightly higher backscattering fractions than experimentally observed (Fig. 6).

The difference between experimentally measured and theoretically predicted energy-loss distributions is in fact very small, particularly when considered over the entire energy range of the outgoing positrons. Figures 14 and 15 illustrate two examples ($\gamma = 60°$ and $\gamma = 0°$) of the full doubly differential positron scattering distributions $d^2\eta/dEd\Omega$, for Au and Al at $\alpha = 60°$. The solid and dashed curves are the MC results convoluted with the SBD detector resolution function [full width at half maximum (FWHM) ~11 keV]. The agreement between MC and experiment lends credibility to the preconvolution MC histogram, shown for the $\gamma = 60°$ case only. This result illustrates the sharply peaked (particularly for Au) elasticlike scattering which dominates in all cases.

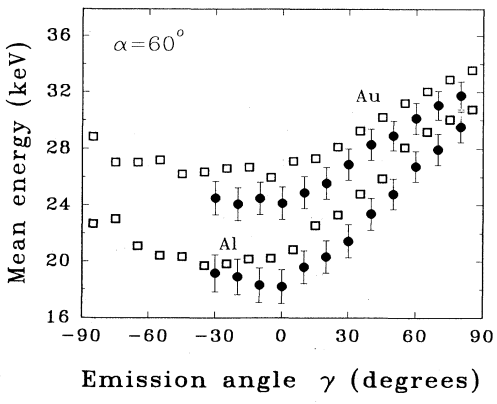

FIG. 13. Mean energy vs emission angle γ of experimental (●) and MC calculated (□) backscattering distributions for positrons incident at 35 keV and $\alpha = 60°$.

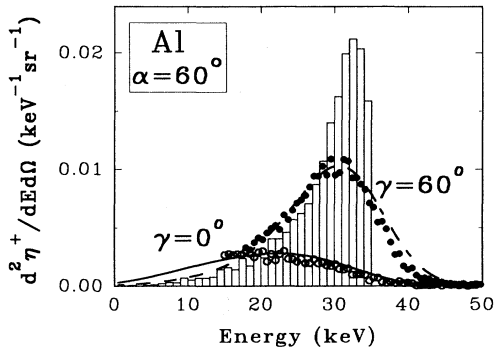

FIG. 14. Doubly differential positron backscattering probabilities, $d^2\eta/dEd\Omega$, for 35-keV positrons incident at $\alpha = 60°$ on Al. Data correspond to emission angles of $\gamma = 0°$ (○) and 60° (●), and are in excellent agreement with MC results that are convoluted with the detector energy resolution. The histogram shows the Monte Carlo results for $\gamma = 60°$ prior to convolution.

VI. PARTICLE HISTORIES

It is possible to use the Monte Carlo process as a tool for studying the interactions within a solid that ultimately lead up to the backscattering of an incident particle. The excellent agreement between experimental and theoretical differential backscattering probabilities reported here allows us to examine the detailed theoretical trajectories with some confidence. Figure 16 shows typical two-dimensional spatial distributions of the trajectories for implanted [16(a)] and backscattered [16(b) and 16(c)] positrons, calculated for 35-keV positrons at normal [16(a) and 16(b)] and 60° [16(c)] incidence on Al. The

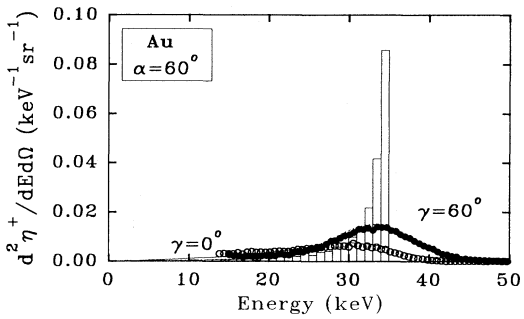

FIG. 15. Same as Fig. 14 for Au.

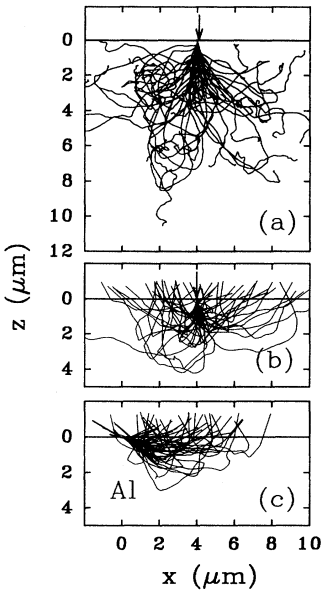

FIG. 16. Monte Carlo trajectories for 35-keV positrons incident on Al. Panel (a) shows trajectories for normally incident ($\alpha=0°$) positrons which stop in the target, while panels (b) and (c) are for those positrons incident at $\alpha=0°$ and $\alpha=60°$, respectively, which are backscattered.

upper figure (and others of this type that have been published elsewhere[35–37]) illustrates that the implantation profile is distributed over a relatively large volume of the sample material, which has long been well known for both positrons and electrons. It is less generally known that a similarly large volume of the target material *also* contributes to those positrons (or electrons) which are backscattered. This fact was illustrated in terms of the mean of the maximum penetration depth $\langle P \rangle$ of backscattered positrons, which was shown in Fig. 2 of Ref. 8 for the case of 35-keV positrons incident at 60° on Al and Au. This information is also contained in Fig. 16, as well as in the mean energy distributions plotted in Figs. 13–15.

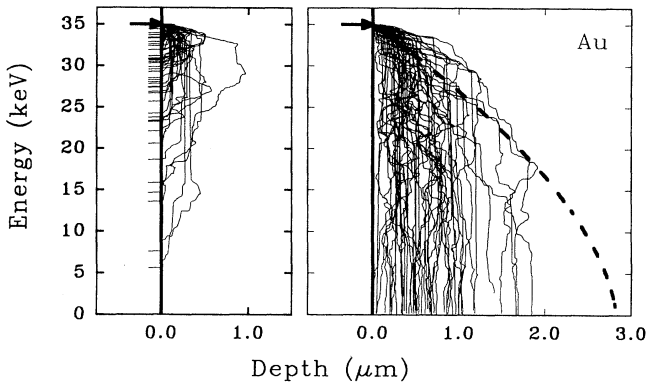

FIG. 18. Phase-space plots for 35-keV positrons incident on Au.

Figures 17 and 18 separate the interactions for backscattered and implanted particles for 35-keV positrons at normal incidence on Al and Au, respectively. In these figures each trajectory is plotted in a modified phase-space representation, or "energy path," which is useful for highlighting some of the details and differences contributing to each ensemble of particles. The right-hand panel of each figure shows the instantaneous kinetic energy as a function of depth in the target material for each positron that eventually stops in the solid. The distribution of each set of energy paths where they end at the bottom of the figure is the implantation profile. The left-hand panel shows the energy paths for each of the backscattered positrons. Each path terminates with a horizontal bar representing its energy when leaving the solid. By inspection of these figures it can be seen that the trajectories for the implanted positrons can be found at depths up to 7 μm, with a most probable depth ~ 3 μm for Al. For Au, the most probable depth is ~ 0.5 μm. This is the "visual" equivalent to the parameter $\langle P \rangle$ described above. By comparison, $\langle P \rangle$ for backscattered positrons is fully half as much, or ~ 1.5 μm for Al and ~ 0.25 μm for Au. In Ref. 8 it was shown that $\langle P \rangle$ (for positrons incident at 60°) was a strong function of the an-

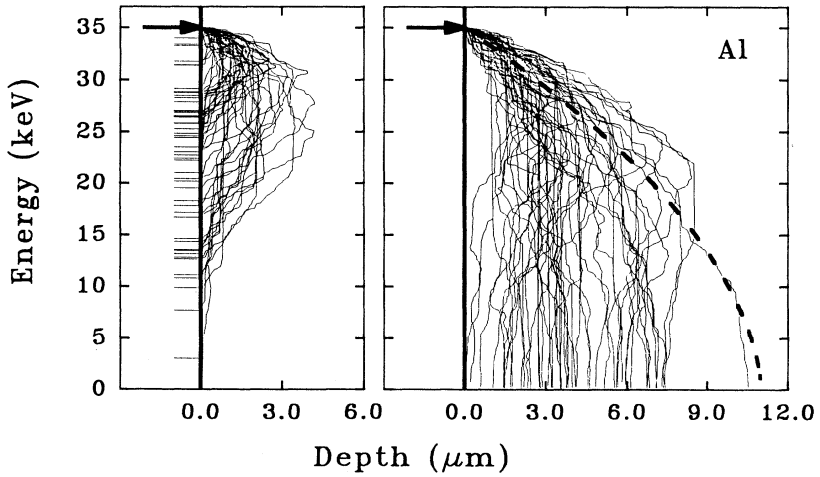

FIG. 17. Phase-space plots of the energy paths for 35-keV positrons incident on Al. The left-hand panel shows the kinetic energy as a function of depth for positrons which ultimately backscatter, where the horizontal lines represent the final energy distribution of the reemitted positrons. The right-hand panel shows those trajectories which stop in the target, where the intersection of the energy paths with the abscissa represents the implantation profile. The dashed curve is the continuous slowing down approximation (CSDA) for energy loss.

gle γ at which the positrons were ejected.

The right-hand panels of Figs. 17 and 18 also show (dashed curve) the predictions of the continuous slowing down approximation (CSDA), as calculated within the Penn formalism that we have used for the inelastic scattering cross sections.[23,26] It is interesting to note that the CSDA describes a reasonable envelope for the energy paths, with allowances for energy-loss straggling. However, the ensemble of trajectories is in general not well represented by the CSDA, which is a straight-line approximation that does not account for deviation (by elastic scattering) from the path penetrating normal to the surface plane. The approximate transport cross sections σ_{tr} for large-angle elastic scattering of 30-keV positrons[26] are $\sigma_{tr} \sim 3 \times 10^{-4}$ Å^2 for Al, and $\sigma_{tr} \sim 5 \times 10^{-3}$ Å^2 for Au. These lead to predicted mean-free paths $\lambda_{tr} = (n\sigma_{tr})^{-1}$, (where n is the atomic density) of ~ 4 and ~ 0.3 μm for Al and Au, respectively. As expected, these distances are on the same order as the distances over which the energy paths in Figs. 17 and 18 are in good agreement with the CSDA approximation.

It was noted in Ref. 8 that a very large number of collisions, on average, contributed to each backscattering event, which is of course consistent with the above observation that a significant fraction of a micron of material is involved. In general, it is the hard elastic collisions that provide the necessary change in direction, and a common view is that only one or two such collisions are important. Figure 19 shows a histogram analysis of elastic collision statistics for 35-keV positrons normally incident on Al. The four panels all plot the number of particles which undergo multiple collisions vs the number of these collisions. The left-hand panels are for very large-angle ($\theta_{el} > 30°$) elastic collisions, while the right-hand panels include all large-angle collisions above $\theta_{el} = 10°$. The top row represents positrons reemitted normal to the surface, $\gamma = 0°$, illustrated by the cartoon to the upper right of the figure, and the lower row is for positrons emitted at $\gamma = 60°$. It is obvious from these data, which are qualitatively similar for the case of Au that the "single-collision" model is far from correct. The backscattered particle distribution is for *all* angles dominated by positrons which have encountered tens of elastic collisions ($\theta_{el} > 10°$), and several that are for very large angles ($\theta_{el} > 30°$).

One of the most interesting features of the experimental data for the angular dependence of backscattered positrons was the evidence (particularly for Al) of a specular-like component when the incident angle α was large. Figure 20 shows a set of elastic-scattering histograms, similar to those in Fig. 19, for 35-keV positrons incident on Al at $\alpha = 60°$. Here it is also evident that a very large number of elastic collisions lead to the backscattered positron distribution, but it can be seen that there is a significant qualitative difference in the number distributions for those positrons emitted at $\gamma = 60°$ (i.e., specular) as compared with those emitted normal to the surface. This difference is not observed in the data for normally incident positrons (Fig. 19), and it suggests that the specular feature arises from the relative absence of very hard elastic collisions. In fact, the *maximum* number of positrons with $\alpha = \gamma = 60°$ have undergone zero collisions with $\theta_{el} > 30°$, as shown in the lower left panel of Fig. 20. Those positrons that are reemitted are on average "gent-

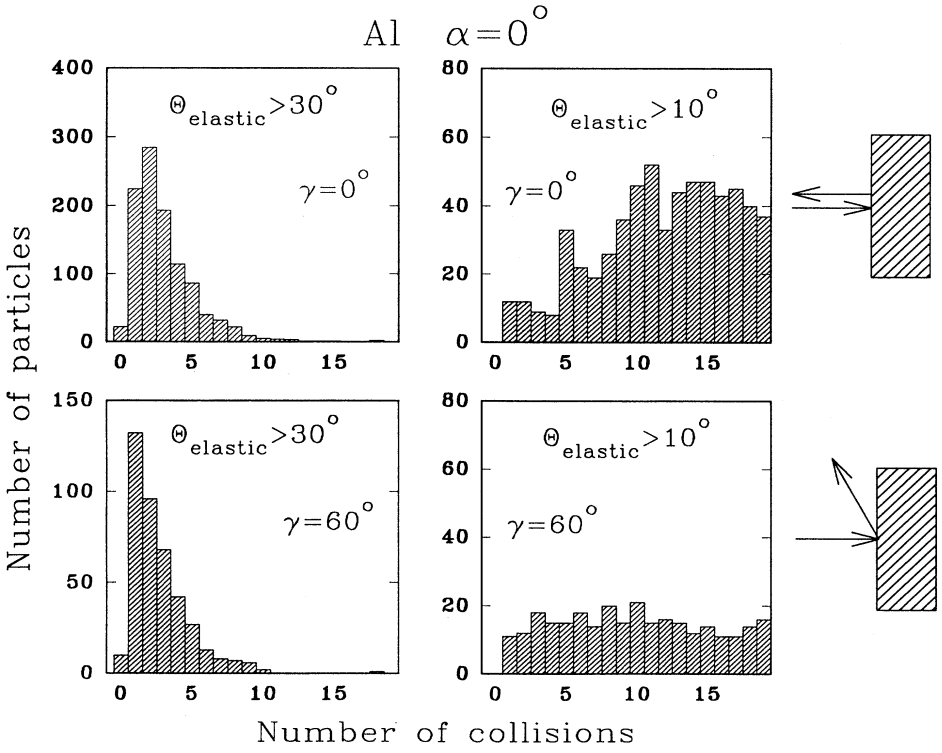

FIG. 19. Histograms of the number of positrons which undergo multiple "hard" elastic scattering collisions prior to backscattering. Data are for 35-keV positrons normally incident ($\alpha = 0°$) on Al, and the plots show both normal ($\gamma = 0°$) and large-angle ($\gamma = 60°$) scattered particles. The two left-hand panels show only the very large-angle collisions, for which $\theta_{el} > 30°$.

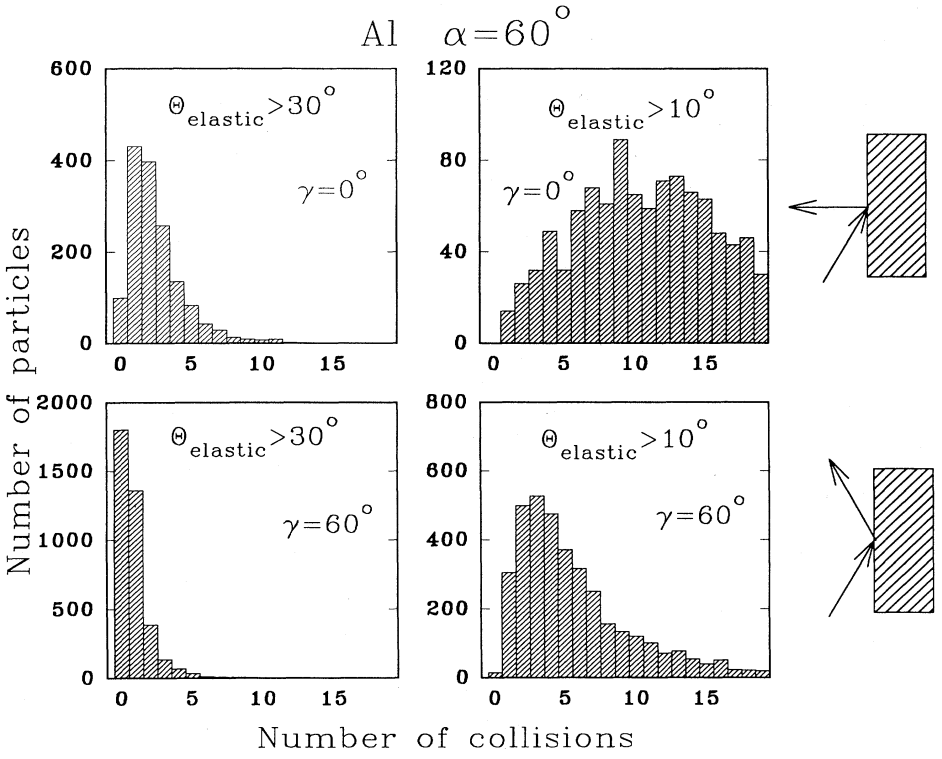

FIG. 20. Elastic-scattering histograms for 35-keV positrons incident at $\alpha=60°$ on Al. Fewer hard collisions contribute to these backscattered positron distributions than for the normally incident case of Fig. 19. This is especially true for the "specularly" reflected positrons shown in the lower two panels, for which the average number of large-angle elastic-scattering events with $\theta_{el}>30°$ is less than 1.

ly" steered by a stochastic multi-interaction process involving only relatively weak inelastic or small-angle elastic collisions.

Figure 21 shows trajectories for 35-keV, $\alpha=60°$ incident positrons that are eventually backscattered from Al. This is the same situation as illustrated in Fig. 16(c), but here only those trajectories are shown which end up at outgoing angles of $\gamma>45°$. The smooth, almost parabolic path characteristic of the steering process discussed above is clearly evident. Analysis of the trajectories for positrons scattered from Au with $\alpha=\gamma=60°$ shows indications of the same type of behavior as we have illustrated here for Al, but the evidence (both in terms of the reduction in hard-angle elastic collisions, and in terms of the parabolic paths) is not nearly as strong. This is consistent with the experimental observations shown in Fig. 9 that specularlike scattering for positrons from Au is observed, but much weaker than for Al (Fig. 8).

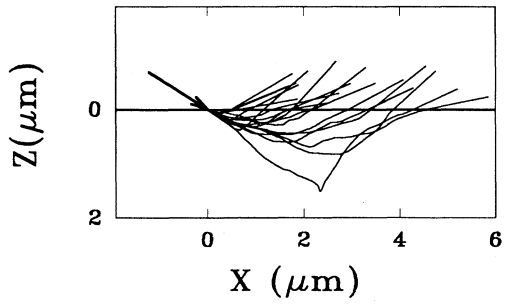

FIG. 21. Spacial trajectories for 35-keV positrons incident at $\alpha=60°$ on Al. Data shown are *only* for those trajectories which lead to positrons backscattered with $\gamma>45°$. The relative absence of large-angle elastic collisions suggested by the histograms in Fig. 20 is responsible for the paraboliclike curves which typify the "average" trajectory. These particles are steered by a continuous and relatively gentle stochastic process of many small-angle elastic collisions.

The relative strength of the specularlike feature for positrons scattered from Al and Au is a direct and tangible demonstration of the influence of elastic scattering, which is for this energy about an order of magnitude stronger for Au than for Al (as reflected in the elastic-scattering transport cross sections, discussed above). The data for backscattered electrons that are also shown in Figs. 8 and 9 show much less specular behavior. This represents significant experimental evidence for a fundamental difference between electrons and positrons, and the result is supported by the stronger elastic-scattering interaction for e^- relative to e^+. Further, we have found that the elastic-scattering difference *alone* is not sufficient to fully explain the e^-/e^+ difference. Without accounting for electron indistinguishability, backscattering distributions calculated for electrons still show more specularlike scattering than is observed experimentally. The addition of exchange plays a role in reducing the relative importance of inelastic-scattering events for electrons.[11,38]

VII. SUMMARY AND CONCLUSIONS

We have presented the results of a comprehensive study of the backscattering of monoenergetic positrons

and electrons from thick solid target materials. Integrated and doubly differential experimental data were studied as a function of incident energy (E) and angle (α), and of target material (Z). Comparisons were made with theoretical Monte Carlo distributions that were calculated without any adjustable parameters, and the agreement was found to be extraordinarily good. On the strength of this, a detailed discussion of the positron-solid interaction was based on the individual trajectories as calculated by the Monte Carlo program.

Much of the data supports expectations, particularly for the case of electrons for which there has been reasonably good data available for some time. However, previous investigations of positron backscattering have not all been consistent. Our experimental and Monte Carlo results for total positron backscattering distributions as a function of Z are in good agreement with the recent data of Mäkinen *et al.*[12] and of Coleman *et al.*,[11] and indicate that η^- is in general $\sim 30\%$ larger than η^+ for all $Z > 20$, with perhaps some evidence for structure in η^+ at $Z \approx 30$. Below $Z = 20$ there is still some uncertainty due to experimental precision, although predictions suggest that the ratio is slightly reduced due to the similarity of electron and positron scattering cross sections for light materials.[11]

Details of the theoretical trajectories for backscattered positrons show that a large volume of the target material is involved, leading to several hundreds of collisions (inelastic and elastic) and significant energy loss. Of particular importance is the finding that the typical backscattered positron undergoes several tens of hard elastic collisions, many of which are $> 30°$. This strongly refutes traditional models based on the assumption that backscattered positrons (or electrons) arise from a single—or a very few—hard elastic collision(s).

Differential experimental data reveal surprisingly strong evidence for specularlike scattering of positrons incident at large ($\alpha > 45°$) angles, which is much more pronounced for the case of Al than for Au. This feature is less important for electron scattering, and is completely absent for electron scattering from Au. It is shown that the specularlike feature arises from particles which undergo many weak elastic collisions, in a gentle stochastic process that is almost entirely free of hard elastic collisions. The intensity of the specular scattering component is inversely correlated with the strength of the elastic interaction. It is also influenced by the relative numbers of elastic-to-inelastic scattering events, which are determined both by material properties and by electron indistinguishability.

In conclusion, it is shown that the basic differences in elastic- and inelastic-scattering cross sections together with the influence of electron exchange are sufficient to describe most of the differences observed in experimental studies of electron and positron backscattering. There are small remaining differences, such as the fact that Monte Carlo calculations consistently predict 1–2% higher total positron backscattering probabilities than those measured experimentally. This could indicate errors in the cross sections, or contributions from effects that are not included in the calculation (such as low-energy positron channeling[39]). In general, however, all such effects play a relatively small role.

ACKNOWLEDGMENTS

The authors are grateful for the technical assistance of I. Schmidt, B. Campbell, and P. Perquin. Funding for this research has been provided by the National Sciences and Engineering Research Council (NSERC) of Canada (W.N.L. and P.J.S.) and by the Network of Centres of Excellence in Molecular and Interfacial Dynamics (P.J.S.).

[1]H. Niedrig, J. Appl. Phys. **53**, R15 (1982).
[2]H. Kanter, Ann. Phys. (Leipzig) (Ser. 6) **6**, 144 (1957).
[3]H. Seidel, Ph.D. thesis, Universität Münster, 1972.
[4]L. Reimer, W. Pöpper, and W. Bröcker, Scanning Electron Microsc. **1**, 705 (1978).
[5]A. Darlinski, Phys. Status Solidi A **63**, 663 (1981).
[6]H. Drescher, L. Reimer, and H. Seidel, Z. Angew. Phys. **29**, (6), 331 (1970).
[7]E. H. Darlington, J. Phys. D **8**, 85 (1975).
[8]G. R. Massoumi, N. Hozhabri, K. O. Jensen, W. N. Lennard, M. S. Lorenzo, Peter J. Schultz, and A. B. Walker, Phys. Rev. Lett. **68**, 3873 (1992).
[9]G. R. Massoumi, N. Hozhabri, W. N. Lennard, and Peter J. Schultz, Phys. Rev. B **44**, 3486 (1991).
[10]J. A. Baker and P. G. Coleman, J. Phys. C **21**, L875 (1988).
[11]P. G. Coleman, L. Albrecht, K. O. Jensen, and A. B. Walker (unpublished).
[12]J. Mäkinen, S. Palko, J. Martikainen, and P. Hautojärvi (unpublished).
[13]T. Tabata, R. Ito, and S. Okabe, Nucl. Instrum. Methods **94**, 509 (1971).
[14]V. A. Kuzminikh, I. A. Tsekhanovski, and S. A. Vorobiev, Nucl. Instrum. Methods **118**, 269 (1974).
[15]N. G. Nakhodkin, A. A. Ostroukhov, and V. A. Romanovskii, Fiz. Tverd. Tela (Leningrad) **4**, 1514 (1962) [Sov. Phys. Solid State **4**, 1112 (1962)].
[16]Z. Radzimski, Acta Phys. Pol. A **53**, 783 (1978).
[17]H. J. August and J. Wernisch, Phys. Status Solidi A **114**, 629 (1989).
[18]G. R. Massoumi, W. N. Lennard, H. H. Jorch, and Peter J. Schultz, in *Positron Beams for Solids and Surfaces (London, Ontario, Canada, 1990)*, edited by Peter J. Schultz, G. R. Massoumi, and P. J. Simpson, AIP Conf. Proc. No. 218 (AIP, New York, 1990), p. 39.
[19]G. R. Massoumi, N. Hozhabri, W. N. Lennard, Peter J. Schultz, S. F. Baert, H. H. Jorch, and A. H. Weiss, Rev. Sci. Instrum. **62**, 1460 (1991).
[20]E. M. Gullikson and A. P. Mills, Jr., Phys. Rev. Lett. **57**, 376 (1986).
[21]K. F. Canter, in *Positron Studies of Solids, Surfaces, and Atoms*, edited by A. P. Mills, Jr., W. S. Crane, and K. F. Canter (World Scientific, Singapore, 1986).
[22]D. W. O. Heddle, J. Phys. E **4**, 981 (1971); D. W. O. Heddle and N. Papadovassilakis, *ibid.* **17**, 599 (1984).

[23]K. O. Jensen and A. B. Walker (unpublished).
[24]D. R. Penn, Phys. Rev. B **35**, 482 (1987).
[25]*Handbook of Optical Constants of Solids,* edited by E. D. Palik (Academic, Orlando, 1985).
[26]K. O. Jensen, A. B. Walker, and N. Bouarissa, in *Positron Beams for Solids and Surfaces (London, Ontario, Canada, 1990),* edited by Peter J. Schultz, G. R. Massoumi, and P. J. Simpson, AIP Conf. Proc. No. 218 (AIP, New York, 1990), p. 19.
[27]F. Arnal, P. Verdier, and P. D. Vincensini, C. R. Acad. Sci. **268**, 1526 (1969).
[28]G. Neubert and S. Rogaschewski, Phys. Status Solidi A **59**, 35 (1980).
[29]P. U. Arifov, A. R. Grupper, and H. Alimkulov, in *Positron Annihilation,* edited by P. G. Coleman, S. C. Sharma, and L. M. Diana (North-Holland, Amsterdam, 1982), p. 699.
[30]K. F. J. Heinrich, Appl. Spectrosc. **22**, 395 (1968).
[31]A. Bisi and L. Braicovich, Nucl. Phys. **58**, 171 (1964).
[32]H. H. Seliger, Phys. Rev. **88**, 408 (1952).
[33]I. K. MacKenzie, C. W. Schulte, T. E. Jackman, and J. L. Campbell, Phys. Rev. A **7**, 135 (1973).
[34]L. R. Logan, M. G. Cottam, Peter J. Schultz, and H. H. Jorch, in *Positron Annihilation,* edited by L. Dorikens-Vanpraet, M. Dorikens, and D. Segers (World Scientific, Singapore, 1988), p. 300.
[35]L. C. Feldman and J. W. Mayer, *Fundamentals of Surface and Thin Film Analysis* (North-Holland, Amsterdam, 1986), p. 141.
[36]D. C. Joy, Scanning Microsc. **5**(2), 329 (1991).
[37]S. Valkealahti and R. M. Nieminen, Appl. Phys. A **35**, 51 (1984).
[38]J. C. Ashley, J. Appl. Phys. **69**, 674 (1991).
[39]P. J. Schultz, L. R. Logan, T. E. Jackman, and J. A. Davies, Phys. Rev. B **38**, 6369 (1988).